Photoelectron momentum distributions of the hydrogen molecular ion driven by multicycle near-infrared laser pulses

Mitsuko Murakami and Shih-I Chu

Phys. Rev. A **94**, 043425 — Published 28 October 2016

DOI: 10.1103/PhysRevA.94.043425

Photoelectron Momentum Distributions of the Hydrogen Molecular Ion Driven by Multi-cycle Near-infrared Laser Pulses

Mitsuko Murakami[1,*] and Shih-I Chu[1,2]

[1]*Center for Quantum Science and Engineering, Department of Physics,*
National Taiwan University, Taipei 10617, Taiwan
[2]*Department of Chemistry, University of Kansas, Lawrence, Kansas 66045, USA*

Abstract

The photoelectron momentum distributions (PMDs) of the hydrogen molecular ion H_2^+ driven by strong near-infrared laser pulses are studied based on the *ab initio* numerical solution of the time-dependent Schrödinger equation and the Volkov wave propagation. Both linear and circular polarization are considered, in accordance with the recent experiment by Odenweller *et al* [Phys. Rev. A **89**, 013424 (2014)]. We will discuss the difference between the molecular (diatomic) and the atomic PMDs, and the effect of molecular potential to the photoelectron energy. In particular, we demonstrate that the above-threshold ionization spectra of H_2^+ could upshift their energy when driven by a linearly polarized laser field in parallel to the molecular axis.

---

[*] mitsuko@phys.ntu.edu.tw

I. INTRODUCTION

The hydrogen molecular ion (H_2^+) is the simplest diatomic molecule, and its interaction with a strong laser pulse has been studied extensively in recent years as a prototype of single-active-electron molecular quantum dynamics. Experimentally, the photoelectron momentum distribution (PMD) of H_2^+ upon the double ionization of H_2 gas was measured using circularly polarized synchrotron radiation in 2007 [1]. Their measurements revealed the rotation of PMDs around the propagation axis of a driving laser field (a.k.a. Coulomb asymmetry), commonly found in atomic PMDs [2]. The fully three-dimensional (3D) time-dependent Schrödinger equation (TDSE) calculation of H_2^+ in the following year confirmed the Coulomb asymmetry, and showed in addition that the two-center interference of ionizing electron from diatomic molecules is better observed with a linearly polarized field [3, 4]. The benchmark 3D-TDSE calculation of H_2^+ including the nuclear motion, subject to linearly-polarized XUV laser pulses (50 $\sim$ 630 eV), was then performed using the 480-core supercomputer in 2009 [5]. It showed that the PMD of H_2^+ resulting from the single-photon absorption of energy $\hbar\omega$ should have (i) a peak at the radius $p = \sqrt{2(\hbar\omega - I_p)}$, where I_p is the ionization potential of H_2^+, and (ii) two-center interference minima at angles $\theta_p = \sin^{-1}(\lambda_e/R)$, where $\lambda_e \equiv 2\pi/p$ and R are the de Broglie wavelength of a photoelectron and the internuclear distance of H_2^+, respectively. The two-center interference in the H_2^+ PMD driven by the XUV field was further investigated in Refs. [6] and [7] based on the fixed-nuclei 3D-TDSE. Note that the two-center interference is a quantum phenomenon, and it is observable only if the condition $\lambda_e \leq R$ is met. For the equilibrium internuclear distance of $R = 2$ in H_2^+, the corresponding photon energy $\hbar\omega$ ($= p^2/2 + I_p$) must be above 164 eV [7].

Meanwhile, the PMD measurements of multi-photon ionization using the near-infrared (NIR, $\sim$800 nm), circularly-polarized laser pulse were made for H_2^+ [8] and H_2 [9]. In these measurements, the kinetic energy release (KER) of proton fragments was coincidentally recorded with the PMD, enabling the determination of internuclear distances R at the time of ionization. Their PMDs exhibited the Coulomb asymmetry whose amount of rotation $\Delta\theta_p$ increased with the internuclear distance R. The 3D-TDSE calculations of H_2^+ in the circularly-polarized laser pulse of intermediate energies (10 $\sim$ 150 nm, $\hbar\omega > I_p$) confirmed the R-dependent Coulomb asymmetry in molecular PMDs [10, 11]. Moreover, the classical trajectory Monte Carlo (CTMC) calculation based on the two-dimensional (2D) model of

H_2^+ in Ref. [12] showed that the rotation angle $\Delta\theta_p$ also increases with the driving laser intensity. Their findings suggest that the Coulomb asymmetry in molecular PMD is a both structural and dynamical effect.

In this paper, we study the PMDs of the H_2^+ molecular ion driven by the 800-nm, 20-cycle ($\sim$ 53 fs) pulse of peak intensity 2×10^{13} W/cm^2. In this low-frequency regime, the PMD would record the ionization dynamics of a diatomic molecule following the multi-photon absorption, leading to the generation of above-threshold ionization (ATI) spectra [13]. Both linear and circular polarization are considered, in accordance with the recent experimental paper by Odenweller *et al* [14]. The calculation is based on the generalized pseudospectral (GPS) method for the solution of the 3D-TDSE [15, 16] and the Volkov-wave propagation in the momentum space [17]. The GPS method has been used previously to study the high harmonic spectra of H_2^+ in linear [16] and circular [18, 19] driving laser fields. This paper complements their results for the PMD and ATI spectra. We will discuss the difference between the molecular (diatomic) and the atomic PMDs, and the effect of the molecular potential in the ATI spectra. Unlike the PMD of single-photon ionizations by XUV pulses, the NIR-driven PMD has multiple peaks at p_s corresponding to the different number of absorbed above-threshold photons ($s = 0, 1, 2, \cdots$) [17]. We will find that the PMDs of the stretched H_2^+ molecular ion driven by a linearly polarized laser pulse exhibit interference minima in each p_s as predicted by the Keldysh-Faisal-Reiss model [20] and may upshift their energies when driven in parallel to the molecular axis [13].

The paper is organized as follows. In Section II, we describe the numerical methods in our calculations. Results are presented in Section III, separately for linear polarization (III A) and for circular polarization (III B). We discuss the difference between the H_2^+ PMD and the atomic PMDs in reference to the helium ion (He^+) and the hydrogen (H) atom, and investigate the photoelectron energy in the ATI spectra in detail. Section IV summarizes the results. Atomic units ($e = m_e = \hbar = 1$) are used throughout, unless specified otherwise.

II. METHODS

A. Time-dependent Schrödinger equation for $\mathbf{H}_2^+$

The *ab initio* treatment of the H_2^+ molecule in a strong laser field requires the solution of the TDSE

$$i\frac{\partial}{\partial t}\psi(\mathbf{r},t) = \left[\mathcal{H}_o + V(\mathbf{r},t)\right]\psi(\mathbf{r},t). \tag{1}$$

The equation is solved using the GPS method in prolate spheroidal coordinates (ξ, η, ϕ) [15]. The internuclear distance is fixed in our calculation (with nuclei at $z = \pm R/2$), but we will investigate solutions for both equilibrium ($R = 2$) and stretched cases ($4 \leq R \leq 7$). The discretized stationary hamiltonian $\mathcal{H}_o$ of H_2^+ is given in Ref. [16]. The interaction potential $V(\mathbf{r},t) = \mathbf{r}\cdot\hat{\mathbf{n}}E(t)$ for a linearly polarized field $E(t) = \sin(\omega_o t)$ along the polarization vector

$$\hat{\mathbf{n}} = (\cos\beta)\hat{\mathbf{z}} + (\sin\beta)\hat{\mathbf{x}}$$

is given by

$$V(\mathbf{r},t) = aE_o(t)\sin(\omega_o t)\left(\xi\eta\cos\beta + \sqrt{(\xi^2-1)(1-\eta^2)}\cos\phi\sin\beta\right), \tag{2}$$

where $E_o(t)$ is an envelope function centered around $t = 0$ and enclosing n cycles, i.e.,

$$E_o(t) = \sqrt{I_o}\cos^2\left(\frac{\omega_o t}{2n}\right). \tag{3}$$

In particular, $\beta = 0$ and $\beta = \pi/2$ give the parallel and the perpendicular fields with respect to the molecular axis, respectively.

An elliptically polarized field is defined as

$$\mathbf{E}(t) = E_o(t)\left[\frac{1}{\sqrt{\varepsilon^2+1}}\sin(\omega_o t)\,\hat{\mathbf{z}} + \frac{\varepsilon}{\sqrt{\varepsilon^2+1}}\cos(\omega_o t)\,\hat{\mathbf{x}}\right], \tag{4}$$

where ε is an ellipticity constant ($0 \leq \varepsilon \leq 1$). In particular, $\varepsilon = 1$ gives the circularly polarized field. In the prolate spheroidal coordinates, the corresponding interaction potential is

$$V(\mathbf{r},t) = E_o(t)a\left[\frac{1}{\sqrt{\varepsilon^2+1}}\xi\eta\cos(\omega_o t) + \frac{\varepsilon}{\sqrt{\varepsilon^2+1}}\sqrt{(\xi^2-1)(1-\eta^2)}\cos\phi\sin(\omega_o t)\right]. \tag{5}$$

B. Volkov Wave Propagation of H_2^+

To eliminate the reflection from the boundary, we split the wave function at a given time t as

$$\begin{aligned}\psi(\mathbf{r},t) &= f(\xi)\psi(\mathbf{r},t) + [1-f(\xi)]\psi(\mathbf{r},t) \\ &= \psi_{(\mathrm{in})}(\mathbf{r},t) + \psi_{(\mathrm{out})}(\mathbf{r},t),\end{aligned} \tag{6}$$

where $f(\xi)$ is an absorbing function that is 1 in the inner region ($1 \le \xi \le \xi_b$) and smoothly decreases ($\sim \cos^{1/8}$) to zero in the outer region ($\xi_b < \xi \le \xi_{\max}$) [21]. For calculations of this paper (800 nm, 2×10^{13} W/cm^2), we let $\xi_b = 37$ and $\xi_{\max} = 74$.

In order to obtain the PMD, the outer wave function is propagated in the momentum space under the Volkov Hamiltonian in the velocity gauge [17]. That is, in each time step, we transform the outer wave function as

$$\tilde{\psi}^{\mathrm{v}}_{(\mathrm{out})}(\mathbf{p},t) = \iiint d^3\mathbf{r}\, \frac{e^{-i[\mathbf{p}+\mathbf{A}(t)]\cdot\mathbf{r}}}{(2\pi)^{3/2}} \psi_{(\mathrm{out})}(\mathbf{r},t), \tag{7}$$

where $\mathbf{A}(t) = \int_t^\infty \mathbf{E}(t')dt'$ is the vector potential, and the superscript v in $\tilde{\psi}^{\mathrm{v}}_{(\mathrm{out})}$ denotes the velocity gauge. The wavefunction $\psi^{\mathrm{v}}_\infty(\mathbf{p},t)$ in the outer space is evolved with the Volkov Hamiltonian

$$\mathcal{H}_\infty(t) = \frac{[\mathbf{p}+\mathbf{A}(t)]^2}{2}, \tag{8}$$

such that

$$\psi^{\mathrm{v}}_\infty(\mathbf{p},t+\Delta t) = e^{-i\mathcal{H}^{\mathrm{v}}_\infty(t)\Delta t}\left[\psi^{\mathrm{v}}_\infty(\mathbf{p},t) + \tilde{\psi}^{\mathrm{v}}_{(\mathrm{out})}(\mathbf{p},t)\right], \tag{9}$$

with an initial condition: $\psi^{\mathrm{v}}_\infty(\mathbf{p},t_0) = 0$. Then, the PMD is evaluated at the end of the time evolution ($t = t_f$) as

$$D(\mathbf{p}) = |\psi^{\mathrm{v}}_\infty(\mathbf{p},t_f)|^2. \tag{10}$$

For a wave function in the outer region ($\xi > \xi_b$), we could approximately write

$$r = a\sqrt{\xi^2+\eta^2-1} \xrightarrow{\xi\gg1} a\xi\,, \tag{11}$$

and

$$\cos\theta = \frac{\xi\eta}{\sqrt{\xi^2+\eta^2-1}} \xrightarrow{\xi\gg1} \eta\,. \tag{12}$$

Therefore, we expand the outer wave function with the spherical harmonics $Y_{\ell m}$ as

$$\psi_{(\mathrm{out})}(\xi,\eta,\phi,t) = \sum_{\ell,m} \varphi_{\ell m}(\xi,t) Y_{\ell m}(\eta,\phi), \tag{13}$$

where

$$\varphi_{\ell m}(\xi,t)=\iint \psi_{(\mathrm{out})}(\xi,\eta,\phi,t)Y_{\ell m}(\eta,\phi)d\Omega\,. \tag{14}$$

Using the spherical-wave expansion:

$$\frac{e^{-i\mathbf{p}\cdot\mathbf{r}}}{(2\pi)^{3/2}}=\sqrt{\frac{2}{\pi}}\sum_{\ell,m}(-i)^{\ell}\mathcal{J}_{\ell}(pr)Y^{*}_{\ell m}(\cos\theta,\phi)Y_{\ell m}(\cos\theta_p,\phi_p), \tag{15}$$

where $\mathcal{J}_\ell(pr)$ are the spherical Bessel functions, and (p,θ_p,ϕ_p) are the spherical coordinates in the momentum space, Eq. (7) becomes

$$\begin{aligned}\tilde{\psi}^{\mathrm{v}}_{(\mathrm{out})}(\mathbf{p},t)\ &\xrightarrow{\xi\gg 1}\sqrt{\frac{2}{\pi}}\sum_{\ell,m}Y_{\ell m}(\cos\theta_p,\phi_p)(-i)^{\ell}\int_1^{\infty}e^{i\mathbf{A}(t)\cdot\mathbf{r}}\varphi_{\ell m}(\xi,t)\mathcal{J}_{\ell}(pa\xi)\,a^2\xi^2d\xi\\ &=\sqrt{\frac{2}{\pi}}\,\mathcal{S}\left\{(-i)^{\ell}\sum_{j}\tilde{\varphi}^{\mathrm{v}}_{\ell m}(\xi(x_j),t)\mathcal{J}_{\ell}(pa\xi(x_j))\,[a\xi(x_j)]^2\,w^{(x)}_{j}a\xi'(x_j)\right\}(\theta_p,\phi_p),\end{aligned} \tag{16}$$

where $\mathcal{S}:(\ell,m)\to(\theta_p,\phi_p)$ is the spherical harmonic transform

$$\begin{aligned}\mathcal{S}\left\{\varphi_{\ell m}(p,t)\right\}(\theta_p,\phi_p)&\equiv\sum_{\ell,m}Y_{\ell m}(\theta_p,\phi_p)\,\varphi_{\ell m}(p,t)\\&=\varphi(p,\theta_p,\phi_p,t)\,,\end{aligned} \tag{17}$$

and

$$\tilde{\varphi}^{\mathrm{v}}_{\ell m}(\xi(x_j),t)\equiv\mathcal{S}^{-1}\left\{e^{-i\mathbf{A}(t)\cdot\mathbf{r}}\ \psi_{(\mathrm{out})}(\mathbf{r},t)\right\}(\ell,m). \tag{18}$$

For calculations in this paper, the number of points used for the inner space in the GPS grid are $N_\xi=150$, $N_\eta=45$ and $N_\phi=91$. The outer space is regularly discretized in the radial direction, i.e., $p_j=j\Delta p$ where $\Delta p=0.05$. In both spaces, the time step is $\Delta t=0.2$.

III. RESULTS

A. Linear Polarization

The kinetic energy of a photoelectron in the adiabatic limit is given by [22]

$$p^2/2=s\,\omega_o+n_o\,\omega_o-I_p-U_p\quad(s=0,1,2,\cdots), \tag{19}$$

where s is the number of above-threshold photons absorbed, I_p is the ionization potential, $U_p = I_o/4\omega_o{}^2$ is the ponderomotive energy, and

$$n_o = \lfloor I_p/\omega_o \rfloor + 1. \tag{20}$$

Accordingly, the PMD driven by a NIR field would have multiple peaks at the radius of

$$p_s = \sqrt{2(s\,\omega_o + n_o\,\omega_o - I_p - U_p)}. \tag{21}$$

In particular for a linearly-polarized monochromatic field, the classical theory predicts the cutoff energy of $2U_p$ for direct ionizations and $10.2U_p$ for back-scattering ionizations [23].

Figure 1 (a) and (b) show the PMD cross section of the H_2^+ molecular ion of a fixed internuclear distance $R = 2$, driven by the linearly polarized 800-nm laser pulse ($\omega_o = 0.057$, $I_o = 2 \times 10^{13}$ W/cm^2, $n = 20$ cycles) in parallel and perpendicular to the molecular axis, respectively. Note that the azimuthal symmetry is broken in (b), but its cross section on the $p_y = 0$ plane should contain most of the electron density because it is in parallel with both the molecular and the laser polarization axes. For a comparison, we plot the PMD cross section of the He$^+$ ion in (c) driven by the same laser pulse along the z-direction. The classical limits corresponding to the cutoff energies of $2U_p$ and $10.2U_p$ are shown as two concentric circles.

We find in Figure 1 that the PMDs are concentrated along the driving-laser axis for all cases (a.k.a. Coulomb focusing), but the molecular PMDs in (a) and (b) have a butterfly-shaped profile and reach higher momentum value than $10.2U_p$. Moreover, the molecular PMD generated by a perpendicular laser field in (b) has a wider profile below the direct-ionization cutoff $2U_p$ than in the back-scattered region above; this may indicate that the photoelectrons in a perpendicular field are less likely to be back-scattered and reach higher energies beyond $2U_p$ than in a parallel field unless they are close to the laser axis.

In the measurement by Odenweller *et al* [14], the PMD of H_2^+ in the 780-nm, linearly polarized field of peak intensity 6×10^{14} W/cm^2 extended up to $|p| = 2.1$, which roughly corresponds to the classical limits of direct-ionization $\sqrt{2(2U_p)} = 2.24$. It is possible that the measurement was not sensitive enough to detect back-scattered photoelectrons of energy $\sim 10.2U_p$, whose intensity is an order of magnitude smaller than directly ionized ones in Figure 1. With an increased sensitivity, it should be possible to observe the butterfly-shaped profile in the H_2^+ PMD at a high driving-laser intensity, distinct from atomic PMDs.

The top panel of Figure 2 shows the corresponding ATI spectra of H_2^+ ($R = 2$), obtained by integrating the cross-sectional PMDs in Figure 1 over angle θ_p and expressing the intensity in logarithmic scale as a function of the kinetic energy on the $p_y = 0$ plane. The classical cutoffs ($2U_p$ and $10U_p$) are indicated with vertical lines. We find that ~~the perpendicular H_2^+ spectra have higher intensity than the parallel, which is consistent to a prediction based on the Keldysh-Faisal-Reiss theory~~ the parallel H_2^+ spectra have higher intensity than the perpendicuar, which is consistent to experiments and the TDSE calculation in Ref. [13]. A comparison with the He^+ spectra shows that the H_2^+ spectra extend far beyond the classical cutoffs, whereas the He^+ spectra fall off rather sharply; this is a reflection of the butterfly-shaped profile in H_2^+ PMDs in Figure 1.

In the bottom panel of Figure 2, the ratio of parallel to perpendicular spectra of H_2^+ at each photoelectron energy is shown. In Ref. [13], it was claimed that this ratio should have a minimum at an energy of $(\pi/R)^2/2$, which is indicated as a vertical line in the plot. Their 3D-TDSE calculation of H_2^+ with a fixed internuclear distance of $R = 3$ did not exhibit such minimum, and neither does ours in Figure 2. This is reasonable given that the de Broglie wavelength condition $\lambda_e \leq R$ was not met in both calculations. For $R = 2$, the photoelectron energy must reach $(2\pi/R)^2/2 = 134$ eV at least to observe such an effect.

An issue overlooked in Ref. [13] was that the parallel and the perpendicular spectra of H_2^+ at $R = 3$ calculated with the same driving-laser wavelength (800 nm) and peak-intensity (2×10^{13} W/cm^2) did not line up, i.e., their spectral peaks appeared at different energies. Notice that Eq. (19) predicts the same energy for both parallel and perpendicular spectra; our result in Figure 2 indeed follows this prediction. In Table I, we list the kinetic energies of a photoelectron from H_2^+ and He^+ given by Eq. (19). When the internuclear distance of H_2^+ stretches beyond the equilibrium distance $R = 2$, however, our TDSE results also deviate from Eq. (19) under certain circumstances, as we will discuss in the rest of this section.

Figure 3 shows the PMD cross section of H_2^+ fixed at larger internuclear distances: (a) $R = 4$, (b) $R = 5$, (c) $R = 6$, and (d) $R = 7$. The driving-laser condition for all cases is the same as in Figure 1, and it is in parallel with the molecular axis ($\beta = 0$). For the internuclear distance $R = 5$ in particular, we also show in (e) the PMD when the same driving laser is oriented in perpendicular to the molecular axis ($\beta = \pi/2$). Also shown in (f) is the PMD of the H atom, which has 4 times smaller ionization potential I_p than He^+, driven by the same laser pulse along the z-axis.

We find in Figure 3 that the PMDs of stretched H_2^+ do not concentrate along the laser polarization axis as much as at the equilibrium distance of $R = 2$ in Figure 1, but instead form concentric rings of radius p_s given by Eq. (21). This change of a PMD profile is due to the relatively ~~higher~~ smaller ionization energy of stretched H_2^+; it is not specific to diatomic molecules but also true for atoms, e.g., compare the He^+ PMD in Figure 1(c) and the H-atom PMD in Figure 3(f) for the same trend. The lower ionization energy seems to introduce interference minima in the PMD in addition, the number of which grows with increasing photoelectron energy. According to the Keldysh-Faisal-Reiss model [20], such interference minima correspond to the nodes of generalized Bessel functions (associated with the Volkov wave solution) along the polar angle θ_p. The number and position of interference minima in the PMD also depend on the initial state configuration from which electron is ionized [26, 27]. In particular for those ionized electrons which are initially in the s-state ($\ell = 0$), a property of generalized Bessel functions demands that the PMD intensity in the perpendicular direction to the driving-laser field (which is $\theta_p = \pm\pi/2$ in Figure 3, except for (e) where $\theta_p = 0, \pm\pi$) should be suppressed at every other p_s, whenever the total number of absorbed photons $s + n_0$ is odd [24]. The PMDs of the stretched H_2^+ molecule in Figure 3 also exhibit this trend, although their ground-state is non-spherical. Note that such interference minima are different from the two-center interference minima discussed in Refs. [24, 25], where H_2^+ was stretched extremely long ($R \geq 20$) as to satisfy the de Broglie wavelength condition $\lambda_e \leq R$. In fact, the kind of interference minima in Figure 3 are not specific to diatomic molecules but also common in atoms, e.g., see the H atom PMD in (f).

In Figure 4, we re-plot the PMD of Figure 3 as a function of polar angles θ_p and the kinetic energy on the $p_y = 0$ plane. In these plots, the interference pattern resembling a set of crossing ripples is clearly visible in between the laser polarization axis. Very similar interference patterns were recorded in the measured PMD of N_2 and O_2 molecules in Ref. [28]. Although our calculation is dependent on the Volkov approximation (and so is the Keldysh-Faisal-Reiss model), we therefore believe it does not affect the correct description of the strong-field photoelectron dynamics. There are a few notable features specific to H_2^+ spectra in Figure 4. First, the spectra along the laser polarization axis ($\theta_p = 0, \pm\pi$) are split into two for $R = 5$ in (b). Second, sidebands are appearing in between the $s = 1, 2, 3, \ldots$ transitions for $R = 6$ in (c).

The location of ATI peaks in Figure 4 is in a good agreement with the photoelectron energies for the $s > 0$ transitions given by Eq. (19), which are listed in Table I, except for the case $R = 5$ in (b). Given that the lowest-order p_s in Figure 3(b) has a node at $\theta_p = \pm\pi/2$, we must assume it is the $s = 0$ spectra corresponding to the absorption of 13 ($= n_0 + s$) odd photons, but its spectral energy in Figure 4(b) seems upshifted by ~ 0.8 eV, about 1/2 the fundamental frequency ω_o, compared to the photoelectron energies in Table I. When the molecular axis is perpendicular to the driving laser field, the ATI peaks for $R = 5$ agrees with Eq. (19), as shown in Figure 4(e). This is further demonstrated in Figure 5, where we plot the parallel and perpendicular ATI spectra for $R = 5$. A misalignment of the two spectra by about $\omega_o/2$ is very clear. We should point out that the same behaviour was present in the previous 3D-TDSE calculation of H_2^+ fixed at $R = 3$ in Ref. [13]; the discrepancy of energy between parallel and perpendicular ATI spectra was also about $\omega_o/2$ in their calculation. This shift of energy in the ATI spectra of H_2^+ driven in parallel with the molecular axis may be related to the field-induced coupling of the lowest-two states (a.k.a. charge resonance) [15, 18, 19], but its exact causes are yet unknown.

B. Circular Polarization

In a circularly-polarized field given by Eq. (4) with $\varepsilon = 1$, the classical limit of the electron momentum is given by [14]

$$p_{\max} = \frac{\sqrt{I_o/2}}{\omega_o}. \tag{22}$$

The corresponding cutoff energy $p_{\max}^2/2$ therefore equals to the ponderomotive energy U_p. The nonzero initial velocity would result in a higher cutoff energy, $8U_p$ [23].

Figure 6(a) shows the PMD cross section on the polarization plane of the H_2^+ at a fixed internuclear distance $R = 2$, driven by the 800-nm, 20-cycle circularly polarized laser field of peak intensity $I_o = 2 \times 10^{13}$ W/cm^2. The classical cutoffs (U_p and $8U_p$) are shown as two concentric circles. For a comparison, the PMD cross section of He^+ driven by the same laser pulse is also shown in (b).

Similar to the PMDs generated by a linearly polarized pulse in the previous section, the PMDs in Figure 6 consist of concentric rings of radius p_s given by Eq. (21). The PMDs driven by a circularly polarized driving laser field are not butterfly-shaped but circular, at least at this driving-laser inetensity. Both H_2^+ and He^+ exhibit a pronounced peak at the first p_s above the classical cutoff $p_{\max} = \sqrt{2U_p}$. Odenweller *et al.* measured the H_2^+ PMD driven by a circularly-polarized 780-nm laser pulse in Refs. [8, 14], and it had a peak at $p = 1.0$. The fact that their PMD peak was located below the classical cutoff ($p_{\max} = 1.6$ at their reported peak intensity of 6×10^{14} W/cm^2) suggests that the effective driving laser intensity was somewhat lower than they claimed, probably around 2×10^{14} W/cm^2. In our calculation, it was necessary to use a 10 times lower peak intensity than theirs to assure the numerical convergence at a reasonable computational cost.

While the PMD of He$^+$ in Figure 6 is uniform in every direction θ_p, reflecting the spherical symmetry of the source atom, the PMD of H_2^+ has gaps along certain axes. This is caused by a symmetry breaking due to the molecular potential. An aligned diatomic molecule has a preferred direction of ionization along the molecular axis, and its PMD tends to be also concentrated along an axis as a result. When the molecular axis is along the z-axis in the configuration space, the PMD is concentrated along the p_x-axis (orthogonal to p_z) in the momentum space. In addition, the long-range Coulomb force slightly rotates the PMD, consistent to the measurements in Refs. [8, 9]. Similar behaviour is known for atoms driven by an elliptically polarized laser pulse, where the preferred axis of ionization corresponds to the major axis of a polarization ellipse [2].

In Figure 7, the PMD cross sections in Figure 6 are re-plotted as a function of polar angle θ_p and the kinetic energy on the $p_y = 0$ plane. We find that the location of the PMD peaks agree with the photoelectron energies given by Eq. (19); see Table I. The lowest-order PMD peak ($s = 1$) of H_2^+ in (a) has a gap along the p_z-axis ($\theta_p = 0, \pm\pi$) and rotated clockwise by about 10 degrees, due to the Coulomb assymetry. For higher-order PMD peaks ($s = 2, 3, \cdots$), the PMD has an additional gap along the p_x-axis ($\theta_p = \pm\pi/2$), so that the PMD has a 4-lobe structure. The energy-resolved PMD measurements of H_2^+ in Refs. [8, 9] also exhibit the 2-lobe and 4-lobe structure at low and high photoelectron energies, respectively, which is in an agreement to our calculation. The gap along the p_z-axis in Figure 7(a) is not surprising and reflects the fact that electrons are preferentially ionizing along the molecular axis because that's where most of the electron density lies. The gap along the p_x-axis, on the other hand, is less intuitive. It implies that there is another preferred direction of ionization for H_2^+ driven by a circularly polarized field, and it is perpendicular to the molecular axis. From a classical viewpoint, the electron positioned on such an axis is at an unstable equilibrium, i.e.,the electron could recombine with either of the two nuclei with equal likelihood. Or else, since the binding energy is minimal along this particular axis, the electron could preferentially escape perpendicular to the molecular axis when driven by a circularly polarized field. Figure 7(a) suggests that this is indeed the likely scenario for higher-order above threshold electrons from the H_2^+ molecular ion.

Though it is desirable to present further calculations with stretched H_2^+, as measured in Refs. [8, 9], our calculation at the moderate resolution does not converge for $R > 2$ for circularly polarized driving laser pulses. Studies of the molecular PMDs in a circularly polarized laser field in the past are based on the 2D H_2^+ model, e.g., the CTMC theory in Ref. [12] or the TDSE in Ref. [9]. They are adequate in reproducing the essential features in experimental PMDs, but we would attempt an *ab initio* calculation in the future.

Finally, Figure 8 shows the ATI spectra obtained by integrating the angle out of the PMD cross sections in Figure 7. Similarly to the ATI spectra driven by the linearly-polarized pulse in Figure 2, the H_2^+ spectra fall much slower than the He^+, highlighting the difference between the molecular and the atomic potentials.

IV. CONCLUSION

To summarize, we studied the PMDs of the H_2^+ molecule driven by a NIR (800 nm) strong (2×10^{13} W/cm^2) laser pulse of linear or circular polarization, based on the GPS solution of the 3D-TDSE (in the limit of fixed nuclear-distance approximation) and the Volkov wave propagation. We find that the H_2^+ PMD at equilibrium distance ($R = 2$) has a butterfly-shaped profile in a linearly polarized field, but it has more circular profile when stretched. The location of ATI peaks mostly follows the adiabatic prediction, except for some particular internuclear distance ($R = 5$) and when driven by a parallel, linearly-polarized laser pulse. Our H_2^+ calculation produced the interference patterns in the PMD similar to the ones experimentally observed in N_2 and O_s molecules and consistent to the Keldysh-Faisal-Reiss model. Our calculation with a circularly-polarized laser pulse needs further improvement in order to fully explain the experimental results in Refs. [8, 9].

ACKNOWLEDGMENTS

This work was partially supported by the Chemical Sciences, Geosciences and Biosciences Division of the Office of Basic Energy Sciences, Office of Science, U. S. Department of Energy.

We also are thankful for the partial support of the Ministry of Science and Technology of Taiwan and National Taiwan University (Grants No. 105R891401 and No. 105R8700-2).

[1] D. Akoury, K. Kreidi, T. Jahnke, T. Weber, A. Staudte, M. Schöffler, N. Neumann, J. Titze, L. P. H. Schmidt, A. Czasch, O. Jagutzki, R. A. C. Fraga, R. E. Grisenti, R. D. Muiño, N. A. Cherepkov, S. K. Semenov, P. Ranitovic, C. L. Cocke, T. Osipov, H. Adaniya, J. C. Thompson, M. H. Prior, A. Belkacem, A. L. Landers, H. Schmidt-Böcking, and R. Dörner, Science **318**, 949 (2007).

[2] M. Bashkansky, P. H. Bucksbaum, and D. W. Schumacher, Phys. Rev. Lett. **60**, 2458 (1988).

[3] D. A. Horner, S. Miyabe, T. N. Rescigno, and C. W. McCurdy, Phys. Rev. Lett. **101**, 183002 (2008).

[4] J. Fernandez, F. L. Yip, T. N. Rescigno, C. W. McCurdy, and F. Martin, Phys. Rev. A **79**, 043409 (2009).

[5] S. X. Hu, L. A. Collins, and B. I. Schneider, Phys. Rev. A **80**, 023426 (2009).

[6] K.-J. Yuan, H. Lu, and A. D. Bandrauk, Phys. Rev. A **83**, 043418 (2011).

[7] X. Guan, E. B. Secor, K. Bartschat, and B. I. Schneider, Phys. Rev. A **85**, 043419 (2012).

[8] M. Odenweller, N. Takemoto, A. Vredenborg, K. Cole, K. Pahl, J. Titze, L. P. H. Schmidt, T. Jahnke, R. Dorner, and A. Becker, Phys. Rev. Lett. **107**, 143004 (2011).

[9] M. Spanner, S. Grafe, S. Chelkowski, D. Pavicic, M. Meckel, D. Zeidler, A. B. Bardon, B. Ulrich, A. D. Bandrauk, D. M. Vileneuve, R. Dorner, P. B. Corkum, and A. Staudte, J. Phys. B: At. Mol. Opt. Phys. **45**, 194011 (2012).

[10] K.-J. Yuan and A. D. Bandrauk, Phys. Rev. A **85**, 053419 (2012).

[11] X. Guan, R. C. DuToit, and K. Bartschat, Phys. Rev. A **87**, 053410 (2013).

[12] K. Doblhoff-Dier, K. I. Dimitriou, A. Staudte, and S. Grafe, Phys. Rev. A **88**, 033411 (2013).

[13] Y. V. Vanne and A. Saenz, Phys. Rev. A **82**, 011403(R) (2010).

[14] M. Odenweller, J. Lower, K. Pahl, M. Schutt, J. Wu, K. Cole, A. Vredenborg, L. P. Schmidt, N. Neumann, J. Titze, T. Jahnke, M. Meckel, M. Kunitski, T. Havermeier, S. Voss, M. Schoffler, H. Sann, J. Voigtsberger, H. Schmidt-Bocking, and R. Dorner, Phys. Rev. A **89**, 013424 (2014).

[15] X. Chu and S.-I. Chu, Phys. Rev. A **63**, 013414 (2000).

[16] D. A. Telnov and S.-I. Chu, Phys. Rev. A **76**, 043412 (2007).

[17] M. Murakami and S.-I. Chu, Phys. Rev. A **93**, 023425 (2016).

[18] K. N. Avanaki, D. A. Telnov, and S.-I. Chu, Phys. Rev. A **90**, 033425 (2014).

[19] K. N. Avanaki, D. A. Telnov, and S.-I. Chu, Phys. Rev. A **92**, 063811 (2015).

[20] H. R. Reiss, Phys. Rev. A **22**, 1786 (1980).

[21] J. L. Krause, K. J. Schafer, and K. C. Kulander, Phys. Rev. A **45**, 4998 (1992).

[22] S. Basile, F. Trombetta, and G. Ferrante, Phys. Rev. Lett. **61**, 2435 (1988).

[23] K.-J. Yuan and A. D. Bandrauk, Phys. Rev. A **84**, 013426 (2011).

[24] T. Zuo, A. D. Bandrauk, and P. B. Corkum, Chem. Phys. Lett. **259**, 313 (1996).

[25] J. Henkel, M. Lein, and V. Engel, Phys. Rev. A **83**, 051401(R) (2011).

[26] Z. Chen, T. Morishita, A.-T. Le, M. Wickenhauser, X. M. Tong, and C. D. Lin, Phys. Rev. A **74**, 053405 (2006).

[27] D. G. Arbo, S. Yoshida, E. Persson, K. I. Dimitriou, and J. Burgdorfer, Phys. Rev. Lett. **96**, 143003 (2006).

[28] A. Gazibegovic-Busuladzic, E. Hasovic, M. Busuladzic, D. B. Milosevic, F. Kelkensberg, W. K. Siu, M. J. J. Vrakking, F. Lepine, G. Sansone, M. Nisoli, I. Znakovskaya, and M. F. Kling, Phys. Rev. A **84**, 043426 (2011).

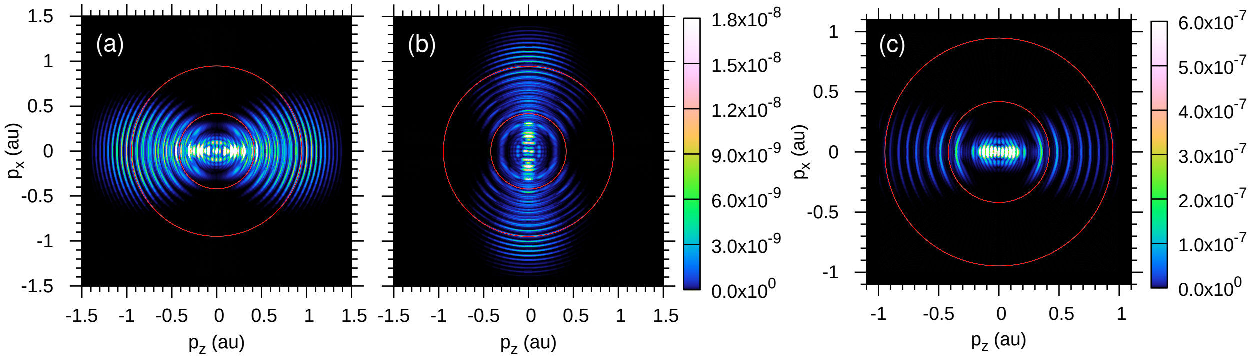

FIG. 1. (Color online) (a) and (b): The PMD cross section of H_2^+, driven by the 800nm, 20-cycle linearly polarized laser field of peak intensity 2×10^{13} W/cm^2 oriented in parallel and perpendicular to the molecular axis, respectively. The same color scale is used for both figures and shown on the right. The internuclear distance is fixed at $R = 2$ along the z-axis in the configuration space. The classical limits corresponding to the cutoff energies of $2U_p$ and $10.2U_p$ are shown as solid lines. (c) The PMD cross section of He$^+$, driven by the same laser field as in (a).

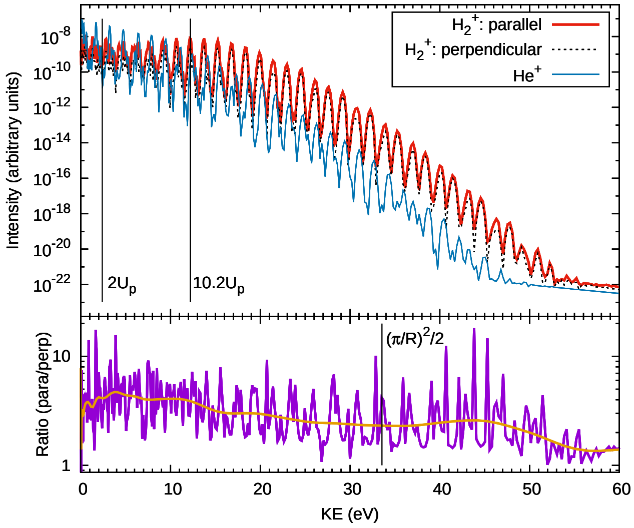

FIG. 2. (Color online) (Top) ATI spectra of H_2^+ (R=2) in parallel and perpendicular to the linearly-polarized 800nm, 20-cycle driving laser pulse of peak intensity 2×10^{13} W/cm^2. Also shown is the ATI spectra of He$^+$. The semiclassical cutoffs of H_2^+ are indicated with vertical lines. (Bottom) Ratio of parallel to perpendicular ATI spectra of H_2^+ in the top panel. The proposed location of two-center interference minimum in Ref. [13] is indicated with a vertical line.

	H_2^+					He^+	H
	R=2	R=4	R=5	R=6	R=7		
I_p	30.0	21.7	19.7	18.5	17.6	54.4	13.6
KE s=0	-0.18	-1.15	-0.75	-1.05	-0.23	0.22	-0.84
s=1	1.37	0.41	0.81	0.50	1.32	1.76	0.71
s=2	2	1.96	2.36	2.05	2.67	3.31	2.26
n_0	20	14	13	12	12	36	9

TABLE I. Ionization energy (I_p) and the kinetic energy (KE) of an photoelectron given by Eq. (19) in eV. Also shown is the integer n_0 defined in Eq. (20).

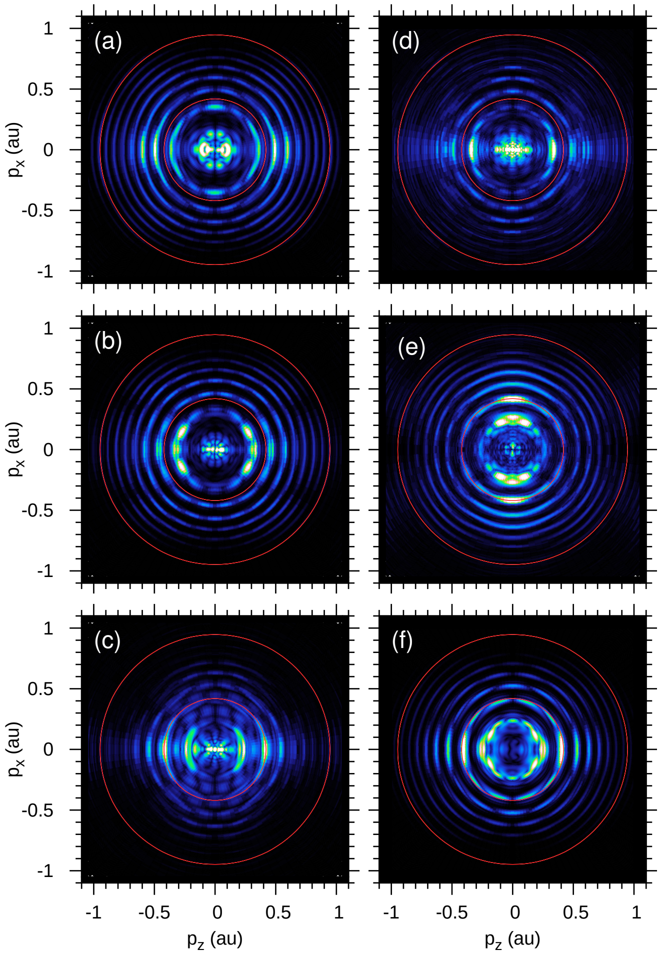

FIG. 3. (Color online) The PMD cross section of H_2^+, driven by the linearly polarized laser field in parallel to the molecular axis (along z), for various fixed internuclear distances: (a) $R = 4$, (b) $R = 5$, (c) $R = 6$, and (d) $R = 7$. All laser parameters are the same as in Figure 1. Color scales are given in the respective plots in FIG. 4. The classical limits corresponding to the cutoff energies of $2U_p$ and $10.2U_p$ are shown as solid lines. (e) The same as (b), but the laser polarization is in perpendicular to the molecular axis. Note that the color scale of (e) is three orders of magnitude smaller than that of (b); cf. Figures 4. (f) The same as (a)-(d), but of the H atom.

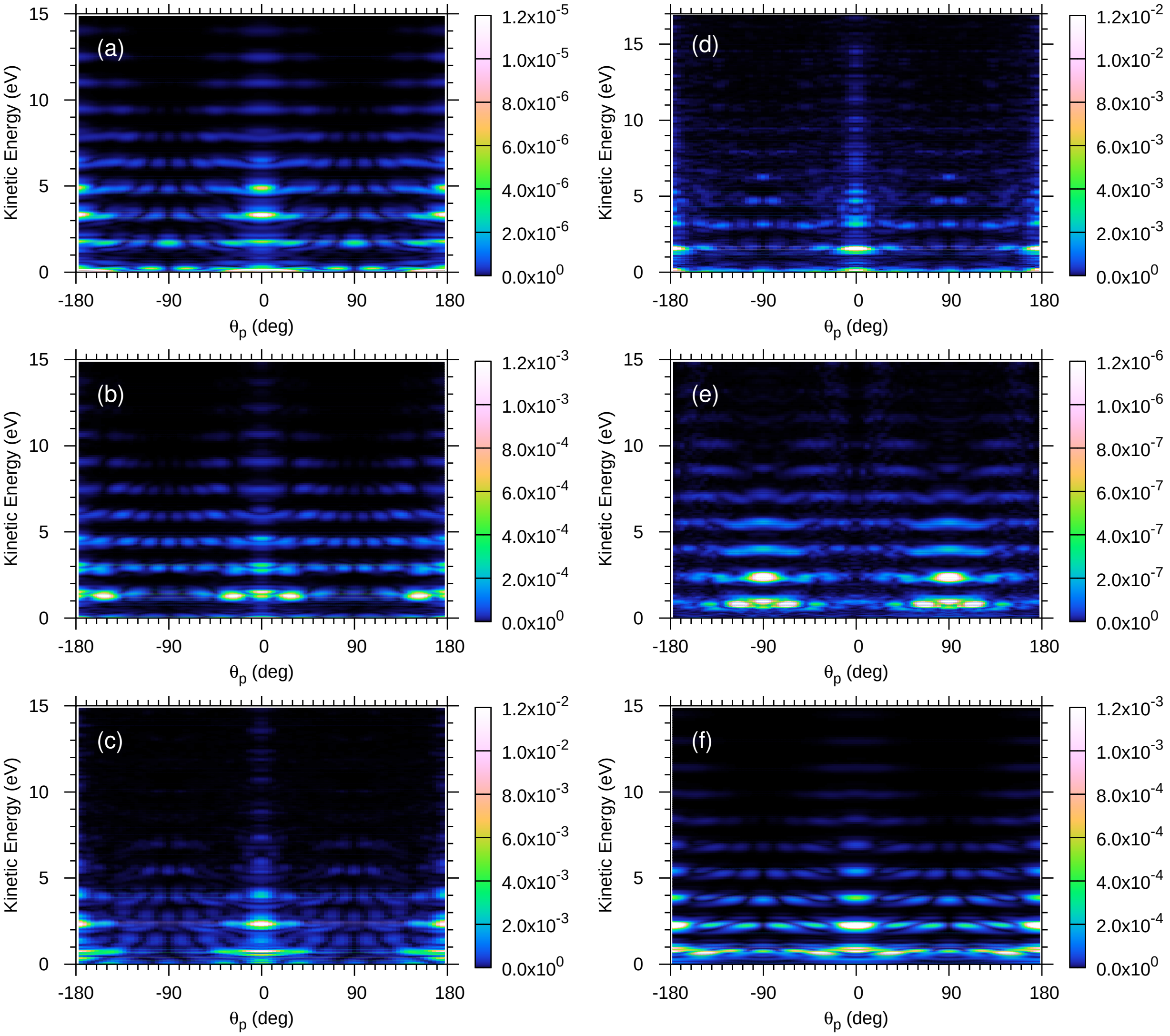

FIG. 4. (Color online) The PMDs in FIG. 3 are shown as a function of polar angle θ_p, defined counter-clockwise from the positive p_z-axis, and of kinetic energy on the cross section ($p_y = 0$).

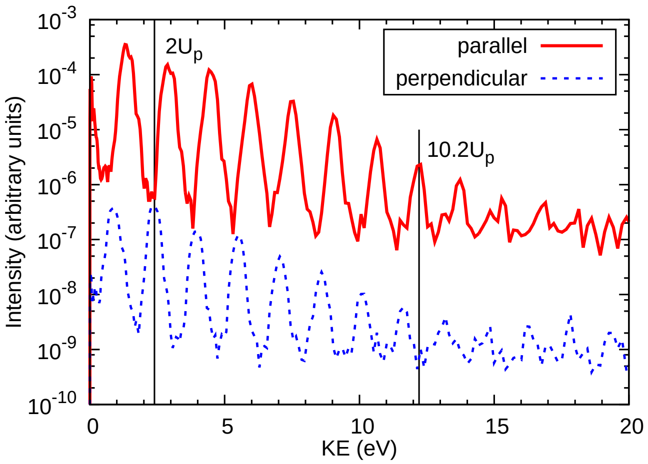

FIG. 5. (Color online) ATI spectra of H_2^+ for $R = 5$, obtained by integrating the angle out of the PMD cross section in Figure 3(b) and 3(e).

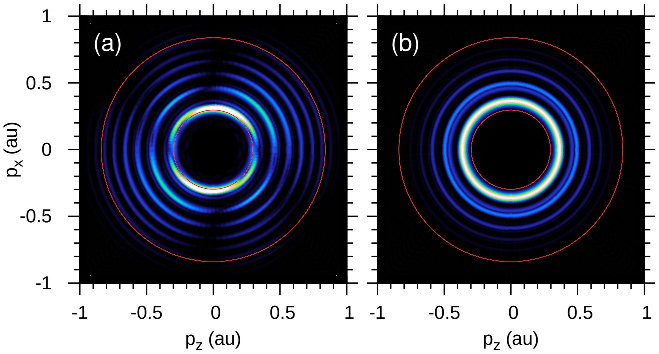

FIG. 6. (Color online) (a) The longitudinal cross section of PMD of H_2^+ at a fixed internuclear distance $R = 2$, driven by the 800nm, 20-cycle circularly polarized laser field of peak intensity 2×10^{13} W/cm^2. Color scales are given in the respective figures in Figure 7. The classical limits corresponding to the cutoff energies of U_p and $8U_p$ are shown as solid lines. (b) The same as (a), but of He$^+$.

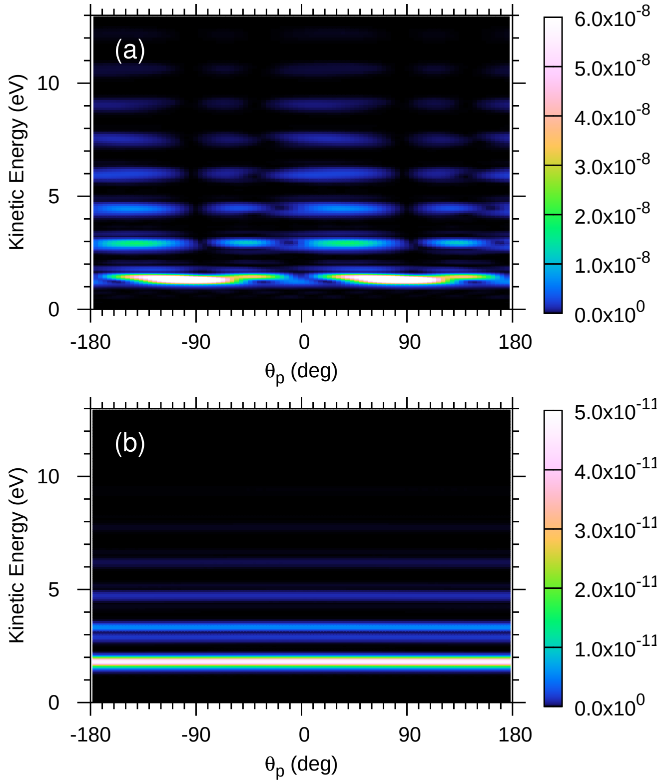

FIG. 7. (Color online) The PMDs in FIG. 6 are shown as a function of polar angle θ_p and the kinetic energy on the cross section.

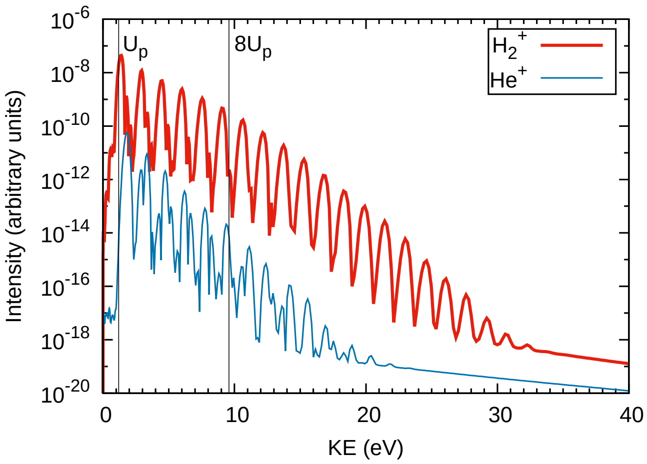

FIG. 8. (Color online) ATI spectra of H_2^+ (R=2) and He^+ driven by the circularly-polarized 800nm, 20-cycle driving laser pulse of peak intensity 2×10^{13} W/cm^2. The semiclassical cutoffs are indicated with vertical lines.